

Synthesis, *in vitro* anticancer activities, and quantum chemical investigations on 1,3-bis-(2-methyl-2-propenyl)benzimidazolium chloride and its Ag(I) complex

Journal of Chemical Research

1–12

© The Author(s) 2020

Article reuse guidelines:

sagepub.com/journals-permissions

DOI: 10.1177/1747519820950219

journals.sagepub.com/home/chl



Goncagül Serdaroğlu¹ , Serap Şahin-Bölükbaşı², Duygu Barut-Celepçi³, Resul Sevinçek³, Neslihan Şahin^{4,5,6}, Nevin Gürbüz^{5,6} and İsmail Özdemir^{5,6}

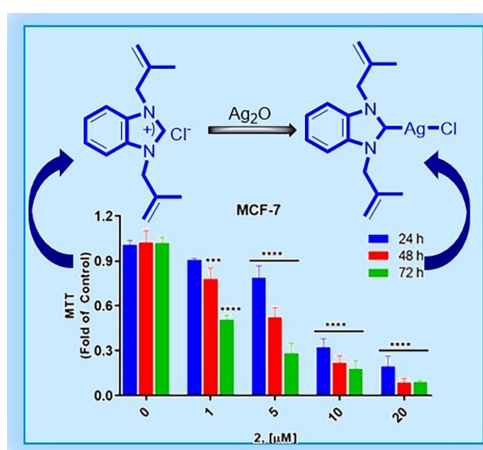
Abstract

1,3-Bis-(2-methyl-2-propenyl)benzimidazolium chloride and its Ag(I) complex are synthesized and the structures are elucidated using spectroscopies techniques. The molecular and crystal structures of the benzimidazolium salt are confirmed by X-ray crystallography. The molecular geometries of the benzimidazolium and its Ag(I) salt are analyzed using the B3LYP functional with the 6–311+G(d,p)/LANL2DZ basis set. The observed Fourier transform infrared and nuclear magnetic resonance isotropic shifts are compared with the calculated values. Besides, the quantum chemical identifiers, significant intramolecular interactions, and molecular electrostatic potential plots are used to show the tendency/site of the chemical reactivity behavior. The three-dimensional Hirshfeld surfaces and the associated two-dimensional fingerprint plots are applied to obtain an insight into the behavior of the interactions in the crystal. Both compounds are tested for their *in vitro* anticancer activities against DU-145 and MCF-7 cancer cells and L-929 non-cancer cells using the 3-(4,5-dimethylthiazol-2-yl)-2,5-diphenyltetrazolium bromide assay.

Keywords

anticancer activity, crystal structure, density-functional theory studies, Hirshfeld analysis, N-heterocyclic carbene

Date received: 16 June 2020; accepted: 23 July 2020



¹Department of Science Education, Faculty of Education, Sivas Cumhuriyet University, Sivas, Turkey

²Department of Biochemistry, Faculty of Pharmacy, Sivas Cumhuriyet University, Sivas, Turkey

³Department of Physics, Faculty of Sciences, Dokuz Eylül University, İzmir, Turkey

⁴Department of Basic Education, Faculty of Education, Sivas Cumhuriyet University, Sivas, Turkey

⁵Department of Chemistry, Faculty of Arts and Sciences, İnönü University, Malatya, Turkey

⁶Catalysis Research and Application Center, İnönü University, Malatya, Turkey

Corresponding author:

Goncagül Serdaroğlu, Department of Science Education, Faculty of Education, Sivas Cumhuriyet University, 58140 Sivas, Turkey.

Email: gserdaroglu@gmail.com



Creative Commons Non Commercial CC BY-NC: This article is distributed under the terms of the Creative Commons

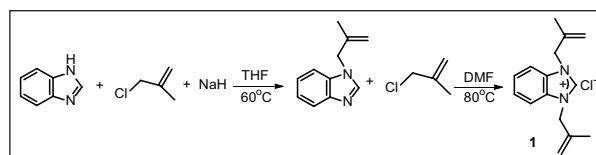
Attribution-NonCommercial 4.0 License (<https://creativecommons.org/licenses/by-nc/4.0/>) which permits non-commercial use, reproduction and distribution of the work without further permission provided the original work is attributed as specified on the SAGE and Open Access pages (<https://us.sagepub.com/en-us/nam/open-access-at-sage>).

Introduction

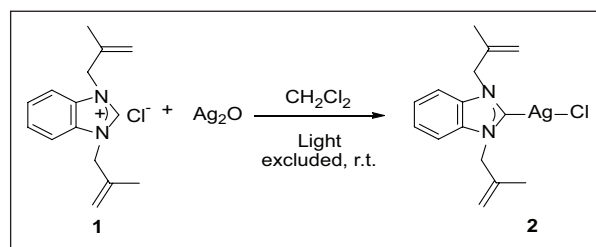
N-heterocyclic carbenes (NHCs) are aromatic organic compounds that contain at least three carbon and two nitrogen atoms. NHCs were first reported by Öfele, Wanzlick, and Schönherr.^{1,2} In general, NHCs are not easy to isolate as single carbene monomers due to their decomposition in the presence of water or their dimerization. All approaches to obtain a stable N-heterocyclic carbene had failed, until Arduengo³ reported the first isolated NHC in 1991. Recently, the use of N-heterocyclic carbenes in coordination chemistry has attracted considerable attention due to their large steric demand and excellent electronic properties, namely, high σ -basicity and low π -acidity,^{4–8} which foster increased activity in catalytic systems.^{9–16} Benzimidazole-based N-heterocyclic carbenes are stable systems and are the subject of significant interest because of pharmacological activities such as antitumor,¹⁷ antibacterial,¹⁸ and antifungal.¹⁹ Most NHCs are prepared by deprotonation of azolium precursors with a simple metal salt or a strong base.^{20,21} Also, NHCs can be obtained from imidazolidine sources.²²

Halide anions have been the subject of increasing research in investigations of both environmental and supramolecular chemistry, since halides are among the most common anions in natural environments. Among halides, chloride plays a vital role in all body fluids because it is responsible for maintaining acid/base balance, transmitting nerve impulses, and so on.^{23,24} In addition, water is an essential molecule in all aspects of human life, so these water–chloride interactions are of fundamental importance to be able to understand solution phenomena, materials chemistry, drug design, catalysis, and atmospheric research.^{25,26} In recent years, monochloride hydrates $[\text{Cl}(\text{H}_2\text{O})_n]^-$ have been extensively investigated using experimental and theoretical techniques, and they have addressed issues such as stability and structure. In addition, the Pt(0) complexes of benzimidazolylidene carbene ligands have been developed and investigated in terms of their ability to catalyze alkene hydrosilylation reactions.²⁷ Recently, the catalytic activity of Pd(II)²⁸ and Co(II)²⁹ complexes of structurally related benzimidazole-based NHCs have been reported. In a study related to different types of Ag(I)–L complexes, the antiproliferative activity of such metal complexes against cancer cells was investigated and the results showed that they had selectivity toward the human breast cancer cells.³⁰

The aim of this paper is to report the preparation and characterization of benzimidazolium salt **1** and its Ag(I)–NHC complex **2**. Characterization was performed using ¹H nuclear magnetic resonance (NMR), ¹³C NMR, and Fourier transform infrared (FTIR) spectroscopies for both compounds. Single-crystal X-ray diffraction was used to elucidate the molecular and crystal structure of the benzimidazolium salt. The X-ray results revealed that the asymmetric unit hosts a cation, a chloride anion, and a water molecule, which are bonded to each other through an intricate hydrogen-bonding network. It was reported that the chloride hydrate structures ($[\text{Cl}_2(\text{H}_2\text{O})_2]_2^-$) in the crystal structure, due to the formation of the hydrogen-bonded cluster, have caused a supermolecular structure.³¹ Crystallographic studies are useful to investigate the



Scheme 1. Synthesis of NHC ligand **1**.



Scheme 2. Synthesis of Ag(I)–NHC complex **2**.

supramolecular assembly of such complexes. Quantum chemical studies were conducted on two compounds to estimate the electronic, spectroscopic, and biological reactivity behavior. With this aim, the geometric structures of the two compounds were predicted, then the assigned NMR shifts and IR assignments of these compounds were compared with the corresponding experimental values. A frontier molecular orbital (FMO) investigation was applied, and molecular electrostatic potential (MEP) diagrams were drawn to estimate/evaluate the chemical reactive behavior/site of two compounds. The *in vitro* anticancer activity of the benzimidazolium salt **1** and the Ag(I) complex **2** was investigated against DU-145 human prostate cancer cells, MCF-7 human breast cancer cells, and mouse L-929 non-cancer adipose cells from the mouse for 24, 48, and 72 h using the 3-(4,5-dimethylthiazol-2-yl)-2,5-diphenyltetrazolium bromide (MTT) assay.³²

Results and discussion

Molecular structures of the NHC ligands and Ag(I)–NHC complexes

NHC ligand **1** was obtained by binding two 2-methyl-2-propenyl units to benzimidazole. The synthesis reaction steps are shown in Scheme 1.

The synthesized NHC ligand **1** and Ag₂O were mixed in dichloromethane with the exclusion of the light to give Ag(I)–NHC complex **2** in excellent yield. The synthetic route is shown in Scheme 2.

The optimized parameters of the compounds were verified by frequency calculations at the B3LYP/6–311+G(d,p)/LANL2DZ are summarized in Table 1. These values were then compared with the experimental values of compound **1** determined by X-ray crystallography. The optimized geometries and atom labeling of each compound are shown in Figure 1.

First, it should be noted that there are small differences between the experimental and computational data because the experimental results were recorded for the solid-state structure of the molecule. From Table 1, the N11–C13 bond length was recorded as 1.321 Å and calculated (for **1** and **2**)

Table 1. The selected geometric parameters of compounds **1** and **2**.

	Exp. ^a	1	2
Bond lengths (Å)			
N11–C13	1.321(3)	1.338	1.357
N11–C1	1.394(3)	1.398	1.396
N11–C16	1.470(4)	1.476	1.470
N12–C13	1.325(4)	1.332	1.357
N12–C2	1.392(3)	1.398	1.397
N12–C25	1.470(3)	1.484	1.470
C1–C2	1.381(3)	1.404	4.402
C2–C3	1.386(3)	1.394	1.394
C3–C4	1.369(3)	1.387	1.392
C4–C5	1.392(3)	1.409	1.405
C5–C6	1.370(3)	1.389	1.392
C6–C1	1.386(3)	1.395	1.394
C16–C17	1.494(4)	1.515	1.516
C17–C20	1.492(4)	1.505	1.505
C17–C24	1.308(4)	1.334	1.334
C25–C26	1.498(4)	1.516	1.516
C26–C33	1.314(4)	1.334	1.334
C26–C29	1.476(4)	1.506	1.505
Bond angles (°)			
C13–N11–C16	126.0(2)	125.3	124.8
C13–N12–C25	126.4(2)	125.9	124.8
N11–C16–C17	112.0(2)	113.4	114.0
N12–C25–C26	111.5(2)	112.6	114.0
C1–N11–C16	125.9(2)	126.8	124.6
C2–N12–C25	125.6(2)	126.2	124.6
C16–C17–C20	123.0(3)	116.8	116.7
C29–C26–C33	123.6(3)	123.5	123.1
C16–C17–C24	120.5(3)	119.6	120.0
C25–C26–C33	120.8(3)	119.3	120.0
Torsion angles (°)			
N11–C1–C2–N12	–0.4(4)	–0.2	0.0
N11–C1–C2–C3	177.4(4)	177.9	179.1
C13–N12–C2–C1	0.3(2)	0.3	0.3
C13–N12–C2–C3	–177.1(2)	–177.5	–178.7
C13–N12–C25–C26	–95.0(3)	–98.7	–110.7
C13–N11–C1–C6	177.2(2)	178.5	178.6
N11–C1–C6–C5	–177.2(3)	–178.0	–178.8
N11–C16–C17–C20	–69.6	–55.7	–54.4
N11–C16–C17–C24	112.4(3)	127.1	128.7
N12–C25–C26–C29	57.7(3)	61.0	55.2
N12–C25–C26–C33	–124.8(3)	–121.6	–127.9

^aThe experimental parameters are based on the single-crystal X-ray structure of compound **1**.

as 1.338 and 1.357 Å. The N11–C16 single bond lengths characterized by single bonding for **1** and **2** were computed as 1.476 and 1.470 Å, with the corresponding experimental bond length being 1.47 Å. In the literature, the C–N bond length and N–C–N bond angle for benzimidazolium chloride hydrate have been observed at 1.4 Å and 111.1°³³ and calculated for the structurally related benzimidazolium chloride at 1.4 Å and 110.8° at the B3LYP/6–311++G(d,p) level of theory.³⁴ Furthermore, the C13–N11–C16 bond angles for **1** and **2** are calculated as 125.3° and 124.8°, which are ~1° different from the observed angle of 126.0°.

Similarly, the C13–N12–C25 bond angle observed at 126.4° for **1** was predicted at 125.9° for **1** and at 124.8° for

2. However, the N11–C16–C17 and N12–C25–C26 bond angles observed at 112.0° and 111.5° were estimated as 113.4° and 112.6° for **1** and as 114.0° for **2**. Here, it should be noted that the calculated angles deviate from the experimental angle value by approximately 2°. However, the C13–N12–C25–C26 dihedral angles for the two compounds were calculated as –98.7° and –110.7°, being almost planar to the ring of each compound, while this angle deviated by 3.7° and 15.7° from the observed value of –95° for **1**. Furthermore, the dihedral angles of N11–C16–C17–C20 for compounds **1** and **2** were calculated as –55.7° and –54.4° with a deviation of –13.9° and –15.2° from the recorded value for **1** of –69.6°. Recently, the C3–C2–C1–N11 and C6–C1–C2–C3 dihedral angles of a structurally related compound were calculated as 179.0°.³⁴ In this study, the same dihedral angle was recorded as 177.4° and calculated as 177.9° for compound **1** and as 179.1° for compound **2**, respectively. Here, it is worth mentioning that the simulated data are in good agreement with the counterparts observed in the experiment, even though there are some differences between them.

Vibrational analysis

The infrared spectra of the NHC **1** and Ag(I)–NHC **2** are presented in Figures S3(a) and (b) in supplemental material; a comparison of the experimental and the scaled theoretical vibrational frequencies can be found in Table S1 (see the supplemental material).

In the literature, the stretching vibrations of the C–H bonds have been reported in the region of 3000–3100 cm^{–1}.^{35–37} In this study, the vibrations of the C–H aromatic stretching (ν_{CH} RA) modes of **1** and **2** occurred at 3113 and 3104 cm^{–1}, whereas the counterparts of these modes for **1** and **2** were simulated in the range of 3113–3088 cm^{–1} and at 3112 cm^{–1}, respectively. Besides, the ν_{as} C–H (ν_{as} C24–H2 and ν_{as} C33–H2) vibrational modes of the carbene parts of **1** and **2** were assigned as 3116 and 3118 cm^{–1}, and 3112 cm^{–1} as a pure mode, whereas the symmetric stretching modes of these groups (νC24–H2 and νC33–H2) were predicted as 3037–3028 cm^{–1} (**1**) and as 3033–3032 cm^{–1} (**2**). The symmetric stretching modes of the methyl groups (νC20–H3 and νC29–H3) for the compounds were recorded as 2937 cm^{–1} (**1**) and as 2914 cm^{–1} (**2**), and assigned in the range of 2926 cm^{–1} (85%)–2916 cm^{–1} (87%) for **1** and as 2927 cm^{–1} (87%) for **2**. From Table S1, the appearing peaks for **1** at 3052 and 3032 cm^{–1} were assigned as the νC24–H2 and νC33–H2 modes calculated at 3037 cm^{–1} (98%) and 3028 cm^{–1} (99%).

The aromatic ring C–C stretching (ν_{CC} RA) mode for **1** was assigned as 1682 cm^{–1} (63%) and 1053 cm^{–1} (72%) as a pure mode, while this mode has a contribution to the bending modes in the spectral region of 1671–427 cm^{–1}. For example, the observed peaks for **1** at 1552, 1186, and 800 cm^{–1} were assigned by potential energy distribution (PED) analysis at 1549, 1176, and 801 cm^{–1} as combined modes with ipb (in-plane bending) HCC RA. However, the ν_{CC} RA mode for **2** was assigned at 1676 cm^{–1} (59%) and 1057 cm^{–1} (56%) as a pure mode, calculated at 1672, 1541, 1534, and 1168 cm^{–1} as a mixed with ipb HCC RA and at 1400 and 818 cm^{–1} as contaminated with the ν_{NC} mode. It

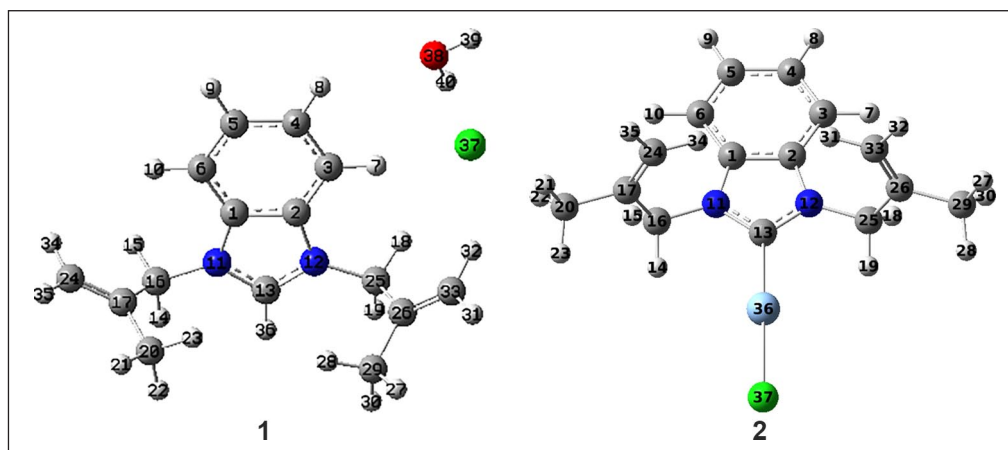


Figure 1. The optimized structures of **1** and **2** at the B3LYP/6-311++G(d,p)/LANL2DZ level in CHCl_3 .

is challenging to predict the NC stretching modes because these modes are generally coupled with C–C stretching modes and with the other stretching modes of the unsaturated ring. In our previous study, the ν_{NC} stretching mode of a benzimidazolium ligand was observed at 1553–1464 cm^{-1} and was predicted to be at 1586–1458 cm^{-1} .³⁸ Here, the observed peaks at 1616 cm^{-1} with a strong IR intensity for **1** was assigned at 1619 cm^{-1} (58%). The ν_{NC} modes for **2** were observed at 1426, 1396, 1377, 1212, 1190, and 800 cm^{-1} and assigned at 1414, 1400, 1379, 1211, 1186, and 813 cm^{-1} , in addition to the assigned modes at 1534, 1446, and 1441 cm^{-1} . Here, the electropositive metal center caused the negative shifts because it attracts electron density.³⁹ In Table S1, it can be seen that the assigned modes at 1446 and 1186 cm^{-1} for **2** are predicted as a pure ν_{NC} mode, and the remaining assigned modes are contaminated with the other vibrational modes.

In this study, the methyl group symmetric bending (umbrella, ν_{CH}) for compounds **1** and **2** was observed at 1441 and 1439 cm^{-1} , respectively. Moreover, the corresponding mode for two compounds was assigned at 1443 cm^{-1} (72%)–1435 cm^{-1} (80%) for **1**, and at 1439 cm^{-1} (60%)–1438 cm^{-1} (74%) for **2**. In the literature, the ν_{CH} (umbrella) mode has been observed at 1424 cm^{-1} ,³⁸ and it is predicted at the B3LYP level as 1368 and 1414 cm^{-1} .³⁸ The scissoring modes (for $\sigma_{\text{C16-H2}}$ and $\sigma_{\text{C25-H2}}$) of the methylene group for compounds **1** and **2** were computed in the ranges of 1527–1477 and 1444–1349 cm^{-1} , respectively, and were observed at 1489 and 1478 cm^{-1} for **1** and at 1478 cm^{-1} for **2**. Moreover, the twisting modes for the same bonds were determined at 1549–1263 cm^{-1} for **1** and at 1441–1231 cm^{-1} for **2**, the wagging modes in the range of 1415–1368 cm^{-1} for **1** and 1441–1231 cm^{-1} for **2**, and the rocking modes were in the range of 984–969 cm^{-1} for **1** and 1268–700 cm^{-1} for **2**. Thus, not only methyl and methylene groups but also the other vibrational modes were in good agreement with both the experimental values and previous reports.

NMR spectral analysis

The NMR shifts for compounds **1** and **2** were obtained using the gauge-independent atomic orbital (GIAO)^{40,41}

approaches to (δ) tetramethylsilane (TMS) [$\delta_{\text{iso}} = \sigma_{\text{TMS}} - \sigma_{\text{iso}}$]. The observed NMR spectra of both compounds are given in Figures S4(a)–(d). The chemical shifts were simulated in CHCl_3 and recorded in CDCl_3 and can be found in Table S2. The correlation equations obtained from regression analysis are given in the supplementary material (Table S2). Accordingly, it can be said that the observed and simulated chemical shifts of both compounds are very comparable with each other; the regression coefficients with regard to the ^{13}C isotropic shifts for compounds **1** and **2** were calculated as $R^2=0.9942$ and $R^2=0.9939$, respectively, whereas ^1H isotropic shifts for these compounds were predicted as $R^2=0.8786$ and $R^2=0.9835$, respectively, in CHCl_3 (Table S2(b)).

Accordingly, the characteristic sharp singlet for the acidic NCHN proton of **1** was observed at 11.75 ppm in the ^1H NMR spectrum. The absence of this peak was also proof of the formation of Ag(I)–NHC **2**. The ^{13}C NMR spectrum of NHC ligand **1** exhibited the characteristic signal of the NCHN carbon at 137.4 ppm. As reported in the literature,^{42–44} this peak was not observed for the Ag–carbene because of the fluxional behavior of the NHC complexes.^{45–47} Furthermore, the chemical shifts of the acidic NCHN proton of the benzimidazolium ligand derivative has been reported at 11.04⁴⁸ and 11.25 ppm.⁴⁹ In a recent study, it was reported that the carbon atom chemical shifts for benzimidazole complexes were reported in the range of 142.6–149.5 ppm.⁴⁸ As expected, the unsaturated ring ^{13}C shifts (atom nos. 1–6 and 13) for compounds **1** and **2** occurred in the ranges of 116.1–137.4 and 116.1–137.5 ppm, whereas they were simulated in the ranges of 118.1–140.4 and 118.4–142.5 ppm in CHCl_3 . Furthermore, the aromatic ^1H shifts for compounds **1** and **2** occurred in the NMR spectra between 7.64–11.75 and 7.39–7.71 ppm, respectively, whereas these shifts were simulated at 7.95–9.40 and 7.64–7.81 ppm (CHCl_3), respectively. Here, it is worth mentioning that the methylene (C16 and C25) and methyl groups (C20 and C29) were responsible for the ^{13}C NMR spectral peaks at 53.5 and 19.7 ppm for **1** and at 55.5 and 19.7 ppm for **2**, respectively. Also, the methylene group protons of these compounds produced the peaks at 5.32 ppm (H27 and H28) for **1** and at 4.99–5.31 ppm (H18 and H19) for **2**.

Natural bond orbital (NBO) analysis

The natural bond orbital analysis and second-order perturbative theory results defined by Weinhold et al.^{50,51} are increasingly used to elucidate the possible intramolecular interactions for a specific organic or inorganic molecular system via the prediction of the electronic parameters such as the stabilization energy ($E^{(2)}$), the donor/acceptor orbital occupancy (q_i/q_j), the donor and acceptor orbital energies (ϵ_i and ϵ_j), and off-diagonal Fock matrix element (F_{ij}). In this study, NBO analysis was applied to elucidate and compare the significant intramolecular interactions of the studied ligand and complex molecules (Table S3).

From Table S3, the possible numbers of intramolecular interactions for **1** are higher than for **2**. Accordingly, the most robust resonance interaction between the donor–acceptor orbital was determined as LP(1) N11 \rightarrow π^* N12–C13 for **1** ($E^{(2)}$ =88.76 kcal/mol) and π C2–N12 \rightarrow π^* N11–C13 for **2** ($E^{(2)}$ =37.84 kcal/mol), respectively, which means that a significant electron density will be present on the antibonding π^* N12–C13 orbital for compound **1** in comparison with the same bond for compound **2**. In other words, the electron delocalization for compound **1** is higher than that of compound **2**, which causes the N12–C13 bond length for compound **1** to be smaller in comparison to the same bond for compound **2**. Here, it is worth remembering that the bond lengths of compounds **1** and **2** were calculated as 1.332 and 1.357 Å, respectively. Moreover, the $E^{(2)}$ value of the resonance interaction occurring in the benzene ring of **1** was calculated in the range of 15.40 and 22.54 kcal/mol; the lowest energy interaction is predicted as π C1–C2 \rightarrow π^* N12–C13 and the highest energy interaction is estimated as π C5–C6 \rightarrow π^* C1–C2. However, the π C1–C2 \rightarrow π^* C3–C4 interaction contributing to the stabilization energy for **2** does not have as much energy as the other interactions occurring in this compound. From Table S3, the highest contribution to the stabilization energy for the benzene ring of **2** has been estimated as then π C5–C6 \rightarrow π^* C3–C4 resonance interaction with an energy of 19.27 kcal/mol and a remarkable orbital occupancy. It can also be seen from Table S3 that there is an anomeric interaction ($n \rightarrow \sigma^*$) for **1** of 12.02 kcal/mol ($ED_j=0.03647e$) for the intramolecular charge transfer from a quite polarizable donor orbital LP(4) Cl to the antibonding orbital σ^* O38–H40. Moreover, the polarity of this orbital has been reduced by the presence of the Ag atom of **2**, and the hybridization of the LP(4) Cl orbital has been calculated to be $sp^{3.52}$. An important interaction occurring in **2** is that of LP(5) Ag \rightarrow π^* N11–C13 with a stabilization energy of 5.06 kcal/mol ($ED_i=1.97270$).

Frontier molecular orbital analysis

FMO investigations have been widely used to provide information on the chemical stability and reactivity tendency of molecular systems via evaluation of the quantum chemical tensors.^{52–55} Table 2 shows the results of the FMO analysis for compounds **1** and **2**.

Accordingly, the ionization energy of the compounds changed as **2** (0.228 au) > **1** (0.191 au) in the gas phase and **2** (0.255 au) > **1** (0.234 au) in $CHCl_3$. The electron affinity

Table 2. The calculated quantum chemical parameters for **1** and **2**.

	Gas		$CHCl_3$	
	1	2	1	2
HOMO (-I)	-0.191	-0.228	-0.234	-0.255
LUMO (-A)	-0.086	-0.067	-0.076	-0.056
ΔE (energy gap)	2.837	4.400	4.293	5.422
X	-3.767	-4.013	-4.216	-4.224
H	1.419	2.200	2.147	2.711
Ω	5.002	3.660	4.139	3.291
ΔN_{max}	2.656	1.824	1.964	1.558

HOMO: highest occupied molecular orbital; LUMO: lowest unoccupied molecular orbital; I: ionization energy; A: electron affinity; X: electronic chemical potential; H: global hardness; Ω : electrophilicity index; ΔN_{max} : charge transfer capability.

The HOMO and LUMO energies are in au; the other parameters are given in eV.

changed as **1** (0.086 au) > **2** (0.067 au) in the gas and **1** (0.076 au) > **2** (0.056 au) in $CHCl_3$. Besides, the energy gap value of each compound rose with an increase in the polarity of the stimulation media. As far as the energy gap values in both the vacuum and the polar environment are concerned, it can be observed that intermolecular interactions for **2** are more likely than in **1** because the ΔE_{gap} for the compounds is calculated as **2** (5.422 eV) > **1** (4.293 eV) in $CHCl_3$ and as **2** (4.400 eV) > **1** (2.837 eV) in the gas phase. However, it can be said that compound **2** is harder than compound **1** for both phases, as expected. As seen from the MEP diagrams and the net charge analysis, compound **2** is more acidic than compound **1** because of the electropositive Ag atom. It is well known that the electron acceptors are Lewis acids and that electron donors are the Lewis bases.⁵⁶ In this study, the electrophilicity index values of the compounds in the $CHCl_3$ (condensed) phase also support the relative acidic characterization. In Table 2, compound **1** (5.002 eV) has a more electrophilic character than compound **2** (3.660 eV) in the gas phase as well as in $CHCl_3$ phase. Furthermore, compound **1** (2.656 eV) has more capability of charge transfer than compound **2** (1.824 eV) in the gas phase. It is well known^{57–60} that the ΔE_{gap} has been commonly used to provide information on the kinetic stability and reactivity of related molecular systems. Thus, the nucleophilicity of compound **2** is greater than compound **1**, which can be the reason for the anticancer activity of compound **2**.

The MEP plots also imply the electrophilic and nucleophilic sites.⁶¹ The positive potential is specified with a blue color which demonstrates the electrophilic attack center, whereas the negative potential is visualized by red, indicating the nucleophilic attack center. In Figure 2, the MEP plot for **1** shows that the negative potential is mostly due to the chloride ion and the water molecule and that the positive potential regions are mainly over the two N atoms belonging to the heterocyclic part of the compound. Similarly, the red color for **2** seems to be mostly over the Cl atom, but it should also be noted that the medium sized-electrostatic potential with the orange color, implying the electrophilic center, is concentrated on the aromatic part of

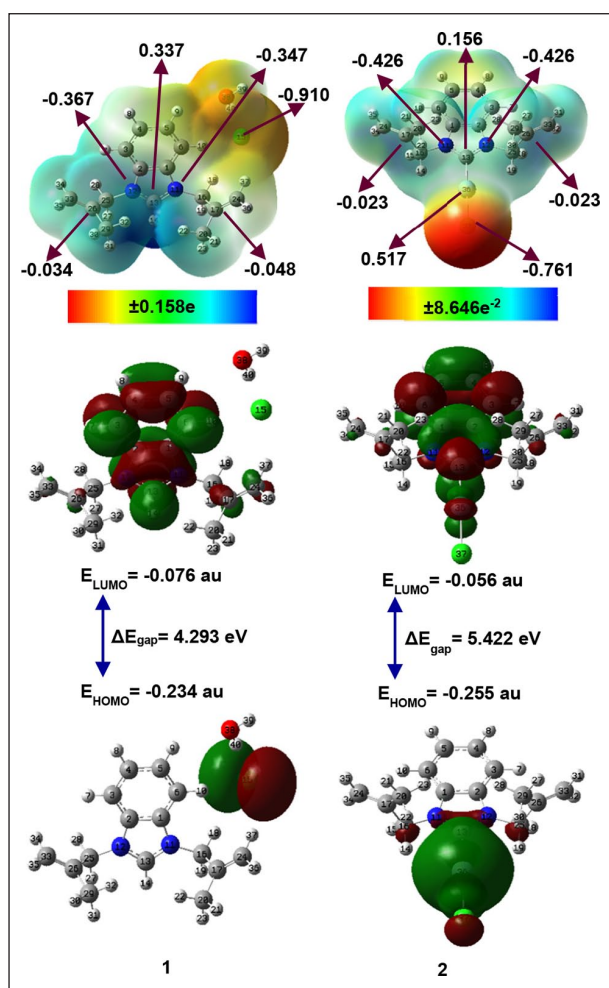


Figure 2. HOMO and LUMO (isoval: 0.02), MEP (isoval: 0.0004) plots, and the NBO charges for selected atoms of compounds **1** and **2** in CHCl_3 . HOMO: highest occupied molecular orbital; LUMO: lowest unoccupied molecular orbital; MEP: molecular electrostatic potential; NBO: natural bond orbital.

2 and the blue color, indicating the nucleophilic center, is over the remaining part of compound **2**. Also, Figure 2 shows the essential net charges obtained from the natural bond orbital calculations; the full atomic charges for both compounds are given in Table S4. Here, the natural atomic charge calculations revealed that the positive charge was located on the electropositive Ag atom as expected; the net atomic charges for the Cl atoms of compound **2** were calculated as +0.517e and -0.761e. However, the net charge for the Cl atom of compound **1** was predicted as -0.910e. The net charges of the N atoms in compounds **1** and **2** were calculated as -0.367e and -0.426e, respectively. Furthermore, the charge distribution over the imidazoline moiety of compound **2** changed due to the presence of the electropositive Ag atom, and the N atom charges for compound **2** are more negative than those of compound **1**.

Hirshfeld surface analysis

Hirshfeld surfaces provide a useful perspective to represent the intermolecular interactions in the crystal structure of a

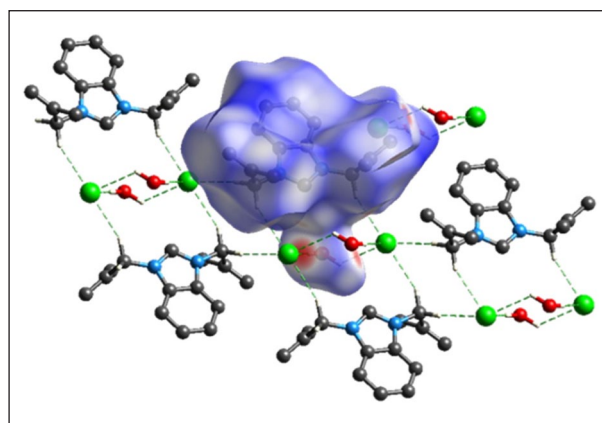


Figure 3. d_{norm} mapped on the Hirshfeld surface for visualizing the intermolecular contacts of compound **1**.

specific molecular system. In this context, the two-dimensional (2D) histograms, known as fingerprint plots, are used to explain the types of intermolecular interactions and show the relative region of the related interactions.^{62,63}

Figure 3 shows the Hirshfeld surfaces for **1** generated using Crystal Explorer (version 17.5), which uses the crystallographic information file (CIF) file as the input.⁶⁴ Then, Hirshfeld surfaces are visualized over the d_{norm} ranges from -0.4522 to 1.3003 Å to give details of the interactions. Accordingly, the most effective interactions, which occurred between the oxygen (O) and chloride (Cl) atoms, are marked as bright red areas. Furthermore, Figure 4 (the 2D fingerprint plots) illustrate the possible contributions of the intermolecular interactions to the Hirshfeld surfaces. Long spikes are characteristic of hydrogen bonds, which represent the $\text{H}\cdots\text{Cl}/\text{Cl}\cdots\text{H}$ type interactions. The left spike (near the d_e axis) represents the interaction of the molecule as a donor, while the other represents as an acceptor. In addition to this interaction, there are two pairs of little wings of the $\text{H}\cdots\text{C}/\text{C}\cdots\text{H}$ type, which represent the $\text{C}-\text{H}\cdots\text{pi}$ type interactions. These $\text{C}-\text{H}\cdots\text{pi}$ type interactions are not strong enough to warrant extensive discussion herein.

In vitro anticancer activities

In this study, three different cell lines were used to determine the anticancer activities of ligand **1** and complex **2**. DU-145 cells are androgen insensitive with high metastatic potential and do not express prostate-specific antigen (PSA). MCF-7 breast cancer cells are ER(+). L-929 non-cancer cells were used to determine the toxicities of ligand **1** and complex **2** in normal cells. The evaluation of the effect of ligand **1** and complex **2** on cancer cell viability was applied using the MTT assay at 24, 48, and 72 h.³² Figure 5(a)–(f) shows the dose and time-dependent anticancer activities of ligand **1** and complex **2** toward the cancer cells and non-tumorigenic cells. The IC_{50} (concentration of the test compound to achieve 50% of cell death) values for the compounds are listed in Table 3 for all the cell lines.

Although the IC_{50} values of ligand **1** against all the tested cell lines were $>20\ \mu\text{M}$ at all the time points, complex **2** showed different IC_{50} values depending on the time and cell line type. Complex **2** did not have IC_{50} values against

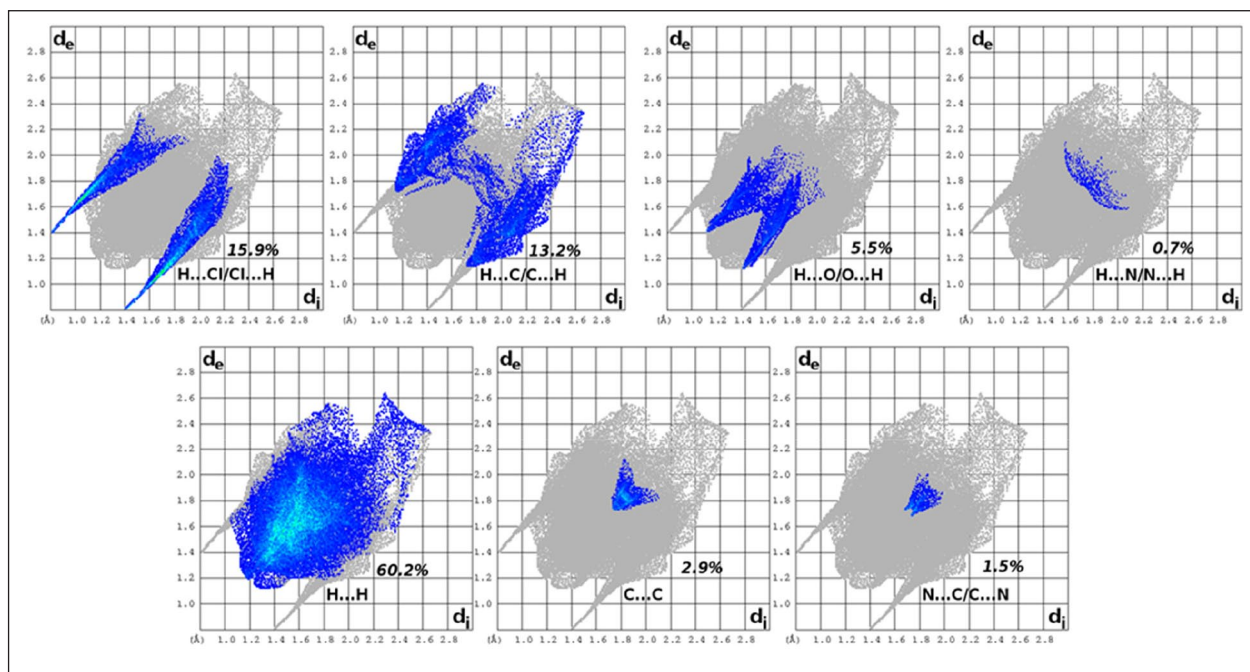


Figure 4. The 2D fingerprint plots of the title compound **1** showing all interactions with the percentage contribution to the total Hirshfeld surface area. The parameter d_i is the closest internal distance from a given point on the Hirshfeld surface, while d_e is the closest external contact.

DU-145 and L-929 cells at 24-h exposure, at least at doses equal to 20 μ M. These results showed that complex **2** had lower IC_{50} values compared to ligand **1**. As lower IC_{50} values indicate higher activity, complex **2** showed higher anticancer activity than ligand **1**. The lowest IC_{50} values were determined against MCF-7 breast cancer cells with complex **2** (13.6, 4.83, and 2.18 μ M after 24, 48, and 72 h exposure, respectively), compared to the DU-145 and L-929 cells. Therefore, MCF-7 breast cancer cells were most susceptible to complex **2**. The selectivity index (SI) values of complex **2** were calculated as >1.47, 2.6, and 2.97 against MCF-7 breast cancer cells and >1.2, and 1.15 against DU-145 prostate cancer cells at 24, 48, and 72 h, respectively. The SI values indicated that complex **2** was more cytotoxic and selective against MCF-7 cells than DU-145 cells. More importantly, complex **2** had higher IC_{50} values for L-929 normal cells and was more cytotoxic toward DU-145 and MCF-7 cancer cells. Therefore, complex **2** demonstrated selectivity between both prostate and breast cancer cells as well as between healthy and cancer cells. Although ligand **1** had no anticancer activity in any cell lines, complex **2** showed dose and time-dependent anticancer activity against all cell lines. More importantly, complex **2** displayed lower anticancer activities on L-929 non-cancer cells than cancer cells.

Conclusion

This paper has focused on the synthesis of benzimidazolium salt and its Ag(I)-NHC complex, and their structural determination, theoretical studies, the comparison of in vitro anticancer activities of both compounds, and the Hirshfeld surface analysis of the benzimidazolium salt. Both compounds were characterized by spectroscopic techniques in addition to characterizing compound **1** by

single-crystal X-ray diffraction. NBO analysis revealed that the main contribution to the stabilization energy lowering was due to the resonance interactions for both compounds; the greatest contribution to the lowering of the stabilization energy was calculated as LP(1) N11 \rightarrow π^* N12–C13 ($E^{(2)}=88.76$ kcal/mol) for **1** and π C2–N12 \rightarrow π^* N11–C13 ($E^{(2)}=37.84$ kcal/mol) for **2**, respectively. Moreover, it can be concluded that compound **2** is more chemically reactive than compound **1** as it has a higher ΔE_{gap} value: the ΔE_{gap} values for the compounds were calculated as **2** (5.422 eV) > **1** (4.293 eV) in CHCl_3 and **2** (4.400 eV) > **1** (2.837 eV) in a vacuum. The in vitro anticancer activities of the compounds were also investigated against DU-145 prostate cancer cells, MCF-7 breast cancer cells, and L-929 non-cancer cells using the MTT cell viability assay for 24, 48, and 72 h. The results showed that complex **2** demonstrated time and dose-dependent anticancer activities toward DU-145 and MCF-7 cancer cells. The results also indicated that ligand **1** had lower anticancer activity against cancer cells compared to the Ag(I) complex **2**. As the lower IC_{50} values indicate higher anticancer activity, complex **2** displays the highest anticancer activity against MCF-7 cell lines at all time points studied. More importantly, complex **2** displayed lower anticancer activity toward L-929 non-cancer cells than cancer cells.

Experimental

Materials and measurements

All experiments were performed under argon in flame-dried glassware using standard Schlenk techniques. All reagents were purchased from Sigma-Aldrich Co. (Dorset, UK). The solvents used were purified by distillation over appropriate drying agents and were transferred under argon.

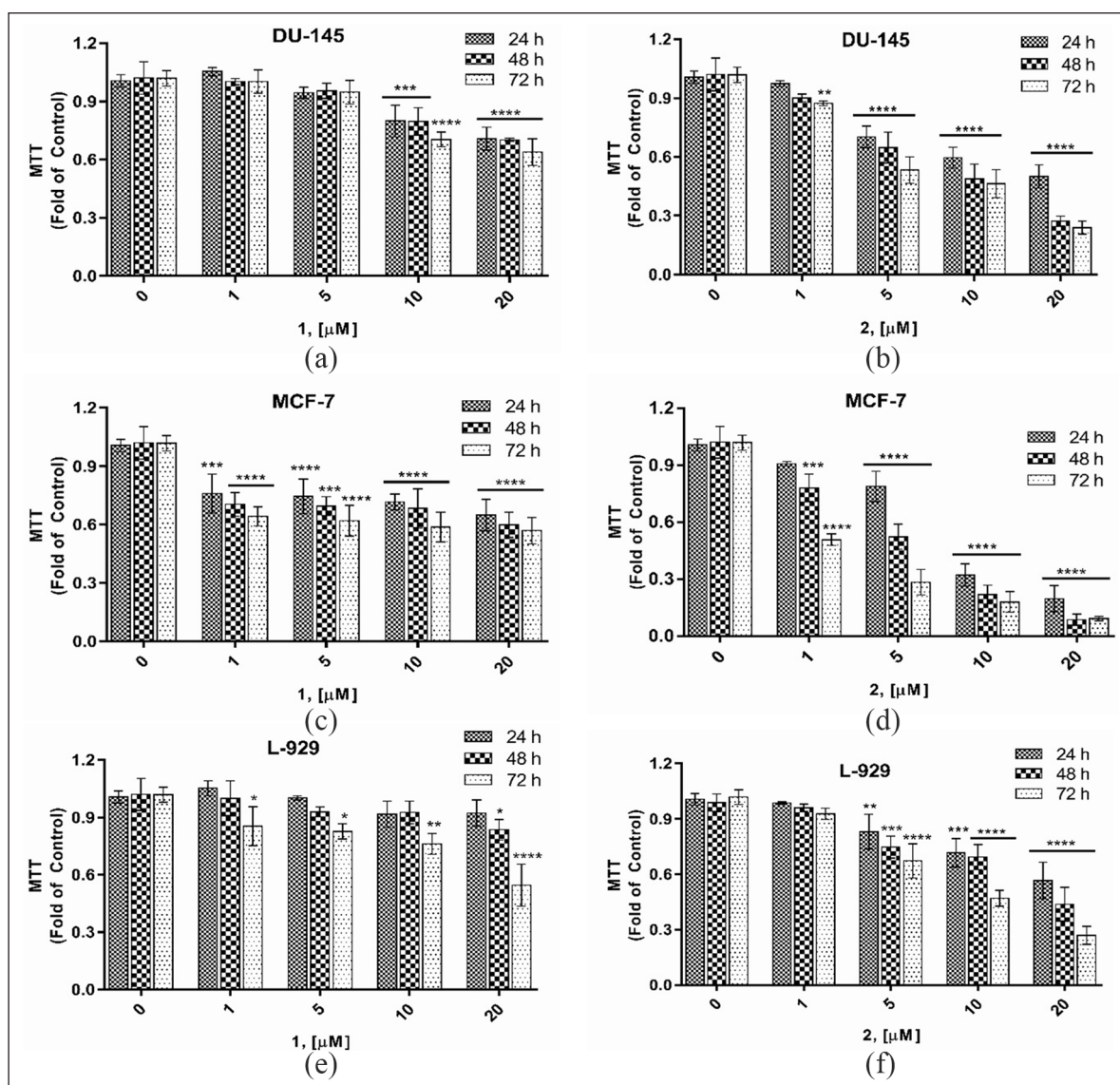


Figure 5. The dose and time-dependence of the *in vitro* anticancer activities of ligand **1** and complex **2** against DU-145 and MCF-7 cancer cells and L-929 non-cancer. Control cells were treated with DMSO. Data are representative of the mean of three separate experiments performed in triplicate and are reported as SEM. (a), (c), (e) *in vitro* anticancer activities of ligand **1** against DU-145, MCF-7 cancer cells and L-929 non-cancer cells, respectively. (b), (d), (f) *in vitro* anticancer activities of complex **2** against DU-145, MCF-7 cancer cells and L-929 non-cancer cells, respectively.

DMSO: dimethyl sulfoxide; SEM: standard error mean.

* $p < 0.05$ versus control, ** $p < 0.005$ versus control, *** $p < 0.0005$ versus control, **** $p < 0.0001$ versus control.

Melting points were determined using an Electrothermal 9100 melting point detection apparatus in capillary tubes, and the melting points are uncorrected. FTIR spectra were recorded in the range of 400–4000 cm^{-1} on a Perkin Elmer Spectrum 100 FTIR. ^1H NMR and ^{13}C NMR spectra were obtained using a Bruker As 400 Mercury spectrometer operating at 400 MHz (^1H) and 100 MHz (^{13}C) in CDCl_3 with TMS as the internal reference. ^1H NMR peaks are labeled as singlet (s) and multiplet (m). Chemical shifts and coupling constants are reported in ppm and Hz, respectively. All the measurements were taken at room temperature using freshly prepared solutions.

Synthesis

NHC ligand **1** and its Ag(I) –NHC complex **2** were prepared under an argon gas atmosphere according to the literature.⁴⁵

1,3-Bis-(2-methyl-2-propenyl)benzimidazolium chloride (**1**)

Benzimidazole (10 mmol) was added to a solution of NaH (10 mmol) in dry tetrahydrofuran (THF) (30 mL) and the mixture was stirred for 1 h at room temperature. 2-Methyl-2-propenylchloride (10.1 mmol) was added dropwise and the obtained solution was heated for 24 h at 60 °C. Next, the solvent was removed under vacuum. Dichloromethane (50 mL) was added to the solid. The mixture was filtered, and the obtained clear solution was concentrated under vacuum. The remaining solution was distilled to give 1-(2-methyl-2-propenyl)benzimidazole. 1-(2-Methyl-2-propenyl)benzimidazole (1 mmol) and 2-methyl-2-propenylchloride (1 mmol) were stirred in dimethylformamide (DMF) (5 mL) for 24 h at 80 °C, and the product precipitated. The solution was filtered and

the solid was rinsed with diethyl ether and dried under vacuum. The crude product was recrystallized from dichloromethane/diethyl ether. Yield: 84%, m.p. 168–169 °C. IR: $\nu_{(\text{CN})}$: 1552 cm^{-1} . ^1H NMR (400 MHz, CDCl_3): δ = 1.90 (s, 6H, $\text{NCH}_2\text{C}(\text{CH}_3)\text{CH}_2$), 4.99 (s, 2H, $\text{NCH}_2\text{C}(\text{CH}_3)\text{CH}_2$), 5.14 (s, 2H, $\text{NCH}_2\text{C}(\text{CH}_3)\text{CH}_2$), 5.32 (s, 4H, $\text{NCH}_2\text{C}(\text{CH}_3)\text{CH}_2$), 7.64–7.65 and 7.75–7.76 (m, 4H, $\text{NC}_6\text{H}_4\text{N}$), 11.75 (s, 1H, NCHN). ^{13}C NMR (100 MHz, CDCl_3): δ = 19.7 ($\text{NCH}_2\text{C}(\text{CH}_3)\text{CH}_2$), 53.5 ($\text{NCH}_2\text{C}(\text{CH}_3)\text{CH}_2$), 113.8 ($\text{NCH}_2\text{C}(\text{CH}_3)\text{CH}_2$), 137.4 (NCHN), 116.1, 127.3, and 131.5 (ArC) and 144.3 ($\text{NCH}_2\text{C}(\text{CH}_3)\text{CH}_2$).

Chloro[1,3-bis-(2-methyl-2-propenyl)benzimidazole-2-ylidene] Ag(I) (**2**)

A solution of Ag_2O (0.5 mmol) and of NHC (1 mmol) ligand **1** in CH_2Cl_2 (25 mL) was stirred at room temperature for

24 h in the dark. Next, the mixture was filtered through Celite. The clear filtrate was evaporated under vacuum to afford the crude product, which was then recrystallized from dichloromethane/diethyl ether. Yield: 79%, m.p. 151–153 °C, IR: $\nu_{(\text{CN})}$: 1378 cm^{-1} . ^1H NMR (400 MHz, CDCl_3): δ = 1.73 (s, 3H, $\text{NCH}_2\text{C}(\text{CH}_3)\text{CH}_2$), 1.80 (s, 3H, $\text{NCH}_2\text{C}(\text{CH}_3)\text{CH}_2$), 4.83 (s, 1H, $\text{NCH}_2\text{C}(\text{CH}_3)\text{CH}_2$), 4.98 (s, 1H, $\text{NCH}_2\text{C}(\text{CH}_3)\text{CH}_2$), 4.99 (s, 2H, $\text{NCH}_2\text{C}(\text{CH}_3)\text{CH}_2$), 5.03 (s, 1H, $\text{NCH}_2\text{C}(\text{CH}_3)\text{CH}_2$), 5.14 (s, 1H, $\text{NCH}_2\text{C}(\text{CH}_3)\text{CH}_2$), 5.31 (s, 2H, $\text{NCH}_2\text{C}(\text{CH}_3)\text{CH}_2$), 7.37–7.40, 7.45–7.48, 7.61–7.64, and 7.69–7.73 (m, 4H, $\text{NC}_6\text{H}_4\text{N}$). ^{13}C NMR (100 MHz, CDCl_3): δ = 19.7 and 20.0 ($\text{NCH}_2\text{C}(\text{CH}_3)\text{CH}_2$), 53.6 and 55.5 ($\text{NCH}_2\text{C}(\text{CH}_3)\text{CH}_2$), 112.1 ($\text{NCH}_2\text{C}(\text{CH}_3)\text{CH}_2$), 113.8 ($\text{NCH}_2\text{C}(\text{CH}_3)\text{CH}_2$), 139.1 ($\text{NCH}_2\text{C}(\text{CH}_3)\text{CH}_2$), 144.3 ($\text{NCH}_2\text{C}(\text{CH}_3)\text{CH}_2$), 114.5, 116.1, 124.3, 127.2, 133.9, and 137.5 (ArC), Ag–C (carbene) not observed.

Table 3. In vitro anticancer activities of ligand **1** and complex **2** against DU-145, MCF-7, and L-929 cells.

Cell lines	Time (h)	IC_{50} (μM) ^a	
		Ligand 1	Complex 2
DU-145 ^b	24	>20	>20
	48	>20	6.20 ± 0.06
	72	>20	5.61 ± 0.03
MCF-7 ^b	24	>20	13.6 ± 0.25
	48	>20	4.83 ± 0.02
	72	>20	2.18 ± 0.01
L-929 ^c	24	>20	>20
	48	>20	12.6 ± 0.19
	72	>20	6.48 ± 0.18

MTT: 3-(4,5-dimethylthiazol-2-yl)-2,5-diphenyltetrazolium bromide; SEM: standard error mean.

Each IC_{50} value represents the mean ± SEM of three independent experiments (nine replicates).

^aCell viability after treatment for 24, 48, and 72 h was determined by MTT staining as described in section “Experimental” (μM).

^bCancer cells.

^cNon-cancer cells.

X-ray crystallography and refinement of **1**

Single-crystal X-ray diffraction data of the NHC ligand were collected at room temperature on a Rigaku–Oxford Xcalibur diffractometer with an electro-optical system (EOS)-charge-coupled device (CCD) detector using graphite-monochromated $\text{MoK}\alpha$ radiation ($\lambda = 0.71073 \text{ \AA}$) with CrysAlis^{Pro} software.⁶⁵ Data reduction and analytical absorption correction were performed using the CrysAlis^{Pro} program.⁶⁶ Utilizing OLEX2,⁶⁷ the structure was solved using the intrinsic phasing method with SHELXT and refined by full-matrix least squares on F^2 in SHELXL.^{68,69} Anisotropic thermal parameters were applied to all non-hydrogen atoms. Hydrogen atoms were placed using standard geometric models and with their thermal parameters riding on those of their parent atoms ($\text{C–H} = 0.93\text{–}0.96\text{–}0.97 \text{ \AA}$). The details of the crystal data and structure refinement of the title compound are given in Table 4.

Crystallographic data as .cif file for the structure reported in this paper have been deposited at the Cambridge Crystallographic Data Center with CCDC 1822823.

Table 4. Crystallographic data and structure refinement parameters for **1**.

Empirical formula	$\text{C}_{15}\text{H}_{21}\text{N}_2\text{OCl}$
Formula weight (g mol^{-1})	280.79
Temperature (K)	294(2)
Crystal system, space group	Triclinic, <i>P</i> -1
<i>a</i> , <i>b</i> , and <i>c</i> (\AA)	9.1633(8), 9.7958(8), and 9.9415(9)
α , β , and γ ($^\circ$)	63.630(9), 78.612(7), and 78.184(7)
<i>V</i> (\AA^3)	776.78(12)
<i>Z</i>	2
Density _{calc} (mg m^{-3})	1.200
Absorption coefficient (mm^{-1})	0.241
<i>F</i> (000)	300
Crystal size (mm)	0.520 × 0.255 × 0.225
Limiting indices	−10 11, −12 10, −12 12
Reflections collected/independent	4756/3139
Parameters	177
Goodness-of-fit on F^2	1.028
Final <i>R</i> indices [$I > 2\sigma(I)$]	$R_1 = 0.053$, $wR_2 = 0.110$
<i>R</i> indices (all data)	$R_1 = 0.085$, $wR_2 = 0.129$
Largest diff. peak and hole (e \AA^{-3})	−0.261/0.303

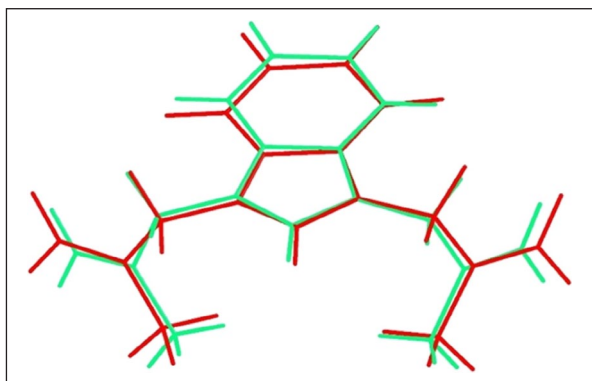


Figure 6. Atom-by-atom superimposition of the calculated structure (red) on the X-ray structure (green) for **1**.

Table 5. Hydrogen-bonding interactions (Å, °) for compound **1**.

D–H...A	D–H	H...A	D...A	D–H...A
O1w–H1wA...Cl1 ⁱ	0.85	2.35	3.182(3)	168
O1w–H1wB...Cl1 ⁱⁱ	0.85	2.58	3.187(3)	129
C8–H8B...Cl1 ⁱⁱ	0.97	2.75	3.668(3)	159
C12–H12A...Cl1 ⁱ	0.97	2.78	3.687(3)	156
C12–H12B...Cl1 ⁱⁱⁱ	0.97	2.72	3.681(3)	173

Symmetry codes: (i) $-1 + x, y, z$; (ii) $1 - x, 2 - y, 1 - z$; and (iii) $1 - x, 1 - y, 1 - z$.

Figure 6 displays the overlay of the X-ray and calculated molecules in the asymmetric unit, which reveals that their structures are virtually equivalent. The root-mean-square deviation (RMSD) value was found to be 0.356 Å with inversion and 0.384 Å without inversion. The crystal structure of the title molecule is consolidated by hydrogen bonds involving the chloride anion, propenyl moieties of the cation, and the water molecule, which are linked through an intricate H-bonding network consisting of two Ow–Hw...Cl and three C–H...Cl interactions (Table 5). Accordingly, the chloride anion behaves as an H-bond acceptor in the crystal structure, resulting in the formation of the one-dimensional supramolecular array (see Figure S1). Besides, the Cl[−] ions were hydrated by forming an anionic hydrogen-bonded cluster [Cl₂(H₂O)₂]^{2−} via the intermolecular O1w–H1wA...Cl1ⁱ and O1w–H1wB...Cl1ⁱⁱ hydrogen bonds. These chloride–water tetrameric clusters have a rectangular-like geometry and generate a *cyclic* R₄²(8) graph-set motif in Etter's graph notation.⁷⁰ They were also held by two cations through the C8–H8B...Cl1ⁱⁱ and C12–H12A...Cl1ⁱ interactions to form a R₄²(12)-type hydrogen-bonded motif, as shown in Figure S2. There is another tetrameric cluster formed by the C12–H12A...Cl1ⁱ and C12–H12B...Cl1ⁱⁱⁱ hydrogen bonds, which reveals the R₄²(8) graph-set notation. All these bifurcated hydrogen bonds are responsible for the stabilization and packing in the supramolecular architecture of the crystal structure.

Density-functional theory studies

The molecular geometries of compounds **1** and **2** were optimized using B3LYP^{71,72} functional and the 6–311+G(d,p)/

LANL2DZ basis set using Gaussian 09W software⁷³ and verified by the non-negative in frequency. The optimized structures of the compound were used for further calculations in both a vacuum and in CHCl₃. The vibrational modes of both compounds have been scaled⁷⁴ with factor of 0.9688 for high frequencies and 1.0189 for low frequencies and assigned by PED analysis using the vibrational energy distribution analysis (VEDA)⁷⁵ program. NMR chemical shifts of both compounds were obtained using the GIAO^{36,37} approach by subtracting the shielding constants of TMS. NBO^{50,51} and FMO^{52–55} analyses were conducted to investigate the intramolecular interactions and biological activity tendency of both compounds. FMO amplitudes and MEP plots provided information on the possible reactive regions of the compounds, and this was visualized using GaussView 6.0.16.⁷⁶ All quantum chemical calculations in the polar environment were performed using the polarized continuum model (PCM).^{77,78}

Cell cultures

The human cancer cell lines DU-145 (HTB-81, human prostate carcinoma), and MCF-7 (HTB-22, human breast adenocarcinoma), were purchased from American Type Culture Collection (ATCC) (Manassas, VA, USA). L-929 (non-cancer cells adipose from mouse) were purchased from European Collection of Animal Cell Culture (ECACC, Salisbury, UK). Eagle's minimum essential medium (EMEM, 30-2003), fetal bovine serum (FBS, 30-2020), and penicillin and streptomycin (30-2300) were purchased from ATCC. Dulbecco's modified Eagle's medium (DMEM, D6429) and trypsin-ethylenediaminetetraacetic acid (EDTA) solution (T-3924) were purchased from Sigma-Aldrich (Sigma-Aldrich Chemie GmbH, Steinheim, Germany).

MTT assay

The MTT method was used to determine the anticancer activity of ligand **1** and complex **2**.³² The DU-145 cell line was cultured in EMEM; MCF-7 and L-929 cells were cultured in the DMEM supplemented with 10% FBS and 1% penicillin/streptomycin solution. All cells were cultured in an incubator with 5% CO₂ at 37 °C. Cells were passaged when the confluence of the cells reached 80% or higher. Cells were seeded in a 96-well plate at a density of 1 × 10⁵ cells/well and allowed to adhere for 24 h at 37 °C in a CO₂ incubator. 1 μL of different concentrations (1–20 μM) of the compounds were added to each well, and the cells were treated for 24, 48, and 72 h. Control and negative control wells were treated with culture medium and sterile DMSO. At the end of the time points, 10 μL of the MTT solution was added to each well and allowed to incubate at 37 °C for a further 2 h. After complete removal of the media, DMSO was added to each well to dissolve the formazan; then, the dye plates were incubated for 15 min at room temperature. Optical density was measured at 570 nm in enzyme-linked immunosorbent assay (ELISA) (Biotek, Epoch, USA). Data represent the average values of three independent measurements with standard error means (± SEM).

Statistical analysis

All experiments were carried out in triplicate, and the results are expressed as means \pm SEM. Data were analyzed using one-way analysis of variance and differences were considered statistically significant at * $p < 0.05$, ** $p < 0.005$, *** $p < 0.0005$, and **** $p < 0.0001$. The IC_{50} values were determined using statistical software, GraphPad Prism7 (GraphPad Software, San Diego, CA, USA).

Acknowledgements

Dokuz Eylül University is acknowledged for the use of the Rigaku–Oxford Xcalibur EoS Diffractometer (purchased under University Research Grant No. 2010.KB.FEN.13). Also, the authors thank Sivas Cumhuriyet University Scientific Research Projects Department (Project No. CUBAP: EĞT-086) and İnönü University Scientific Research Projects Department (Project No. FOA-2018-1135) for their financial support. All calculations were carried out at TUBITAK ULAKBİM, High Performance and Grid Computing Center (TR-Grid e-Infrastructure). In vitro anticancer activity studies were performed at Advanced Technology Research and Application Center (CUTAM), Sivas Cumhuriyet University.

Author contributions

All authors contributed to the study conception and design. Synthesis, 1H NMR, ^{13}C NMR, and FTIR spectra were performed by Neslihan Şahin, Nevin Gürbüz, and İsmail Özdemir. Crystallographic studies were performed by Duygu Barut-Celepci and Resul Sevinçek. Density-functional theory studies were performed by Goncagül Serdaroğlu. Cell culture studies were performed by Serap Şahin-Bölükbaşı. The first draft of the paper was written by Serap Şahin-Bölükbaşı, Goncagül Serdaroğlu, Neslihan Şahin, and Duygu Barut-Celepci. All authors commented on the paper and read and approved the final paper.

Declaration of conflicting interests

The author(s) declared no potential conflicts of interest with respect to the research, authorship, and/or publication of this paper.

Ethical approval

All ethical guidelines have adhered.

Funding

The author(s) received no financial support for the research, authorship, and/or publication of this paper.

ORCID iD

Goncagül Serdaroğlu  <https://orcid.org/0000-0001-7649-9168>

Supplemental material

Supplemental material for this paper is available online.

References

- Wanzlick HW and Schönherr HJ. *Angew Chem Int Ed* 1968; 7: 141.
- Öfele K. *J Organomet Chem* 1968; 12: 42.
- Arduengo AJ III, Harlow RL and Kline MJ. *J Am Chem Soc* 1991; 113: 361.
- Herrmann WA. *Angew Chem Int Ed* 2002; 41: 1290.
- Crudden CM and Allen DP. *Coord Chem Rev* 2004; 248: 2247.
- Díez-González S and Nolan SP. *Coord Chem Rev* 2007; 251: 874.
- Nolan SP. *N-heterocyclic carbenes in synthesis*. London: Wiley, 2006.
- Kantchev EA, O'Brien CJ and Organ MG. *Angew Chem Int Ed* 2007; 46: 2768.
- DePasquale J, White NJ, Ennis EJ, et al. *Polyhedron* 2013; 58: 162.
- Şahin N, Demir S and Özdemir İ. *Arch Org Chem* 2015; 2: 20.
- Lai R, Daran JC, Heumann A, et al. *Inorg Chim Acta* 2009; 362: 4849.
- Van Rensburg H, Tooze RP, Foster DF, et al. *Inorg Chem* 2004; 43: 2468.
- Pizzolato SF, Giannerini M, Bos PH, et al. *Chem Commun* 2015; 51: 8142.
- Berardi S, Carraro M, Iglesias M, et al. *Chem Eur J* 2010; 16: 10662.
- Rouen M, Queval P, Falivene L, et al. *Chem Eur J* 2014; 20: 13716.
- Clavier H, Urbina-Blanco CA and Nolan SP. *Organometallics* 2009; 28: 2848.
- Özdemir İ, Demir S, Şahin O, et al. *Appl Organomet Chem* 2008; 22: 59.
- Schneider H, Schmidt D, Eichhöfer A, et al. *Eur J Inorg Chem* 2017; 19: 2600.
- Betzer JF, Nuter F, Chitichirovsky M, et al. *Bioconjugate Chem* 2016; 27: 1456.
- Haque RA, Asekunowo PO, Razali M, et al. *Heteroatom Chem* 2014; 25: 194.
- Stachowicz J, Krajewska-Kula E, Łukaszuk C, et al. *Indian J Pharm Sci* 2014; 76: 287.
- Jahnke CM and Hahn FE. *Introduction to N-heterocyclic carbenes: synthesis and stereoelectronic parameters*. Cambridge: RSC Publishing, 2011, p. 1.
- National Library of Medicine. *Genetics home reference*. Bethesda, MD: The Library.
- Safin DA, Babashkina MG, Robeyns K, et al. *New J Chem* 2017; 41: 8263.
- Butchard JR, Curnow OJ, Garrett DJ, et al. *Angew Chem Int Ed* 2006; 45: 7550.
- Kopylovich MN, Tronova EA, Haukka M, et al. *Eur J Inorg Chem* 2007; 29: 4621.
- Buisine O, Berthon-Gelloz G, Brière J-F, et al. *Chem Commun* 2005; 30: 3856.
- Şahin N, Gürbüz N, Karabıyık H, et al. *J Organomet Chem* 2020; 907: 121076.
- Şahin N, Yıldırım İ, Özdemir N, et al. *J Organomet Chem* 2020; 918: 121285.
- Çevik-Yıldız E, Şahin N and Şahin-Bölükbaşı S. *J Mol Struct* 2020; 1199: 126987.
- Trzybinski D and Sikorski A. *CrystEngComm* 2013; 15: 6808.
- Skehan P, Storeng R, Scudiero D, et al. *J Natl Cancer Inst* 1990; 82: 1107.
- Şahin N, Kılıç-Cıkla I, Özdemir N, et al. *Mol Cryst Liq Cryst* 2018; 664: 109.
- Serdaroğlu G and Şahin N. *J Mol Struct* 2019; 1178: 212.
- Muthu S and Isac Paulraj E. *Spectrochim Acta A* 2013; 112: 169.
- Eazhilarasi G, Nagalakshmi R and Krishnakumar V. *Spectrochim Acta A* 2008; 71: 502.

37. Serdaroglu and Uludag N. *Bulg Chem Commun (Special Issue I)* 2018; 50: 25.
38. Serdaroglu and Uludag N. *J Mol Struct* 2018; 1166: 286.
39. Asekunowo PO, Haque RA, Razali MR, et al. *Appl Organomet Chem* 2017; 31: e3655.
40. Rohlffing CM, Allen LC and Ditchfield R. *Chem Phys* 1984; 87: 9.
41. Wolinski K, Hinton JF and Pulay P. *J Am Chem Soc* 1990; 112: 8251.
42. Pytkowicz J, Nielsen DJ, Cavell KJ, et al. *Inorg Chim Acta* 2003; 352: 143.
43. Roland S and Mangeney P. *J Org Chem* 2001; 631: 157.
44. Lee HM, Chiu PL, Hu CH, et al. *J Org Chem* 2005; 690: 403.
45. Şahin-Bölükbaşı S, Şahin N, Tahir MN, et al. *Inorg Chim Acta* 2019; 486: 711.
46. Şahin N, Şahin-Bölükbaşı S, Tahir MN, et al. *J Mol Struct* 2019; 1179: 92.
47. Sayin K, Kariper SE, Taştan M, et al. *J Mol Struct* 2019; 1176: 478.
48. O'Beirne C, Althani HT, Dada O, et al. *Polyhedron* 2018; 149: 95.
49. Üstün E, Düşünceli SD and Özdemir İ. *Struct Chem* 2019; 30: 769.
50. Weinhold F, Landis CR and Glendening ED. *Int Rev Phys Chem* 2016; 35: 399.
51. Reed AE, Curtiss LA and Weinhold F. *Chem Rev* 1988; 88: 899.
52. Sheldrick GM. *Acta Crystallogr Sect* 2015; C71: 3–8.
53. Koopmans T. *Physica* 1934; 1: 104.
54. Parr RG, Szentpaly LV and Liu S. *J Am Chem Soc* 1999; 121: 1922.
55. Parr RG and Pearson RG. *J Am Chem Soc* 1983; 105: 7512.
56. Pearson RG. *Proc Natl Acad Sci USA* 1986; 83: 8440.
57. Yang W and Parr RG. *Proc Natl Acad Sci USA* 1985; 82: 6723.
58. Fleming I. *Frontier orbitals and organic chemical reactions*. London: John Wiley & Sons, 1976.
59. Kim KH, Han YK and Jung J. *Theor Chem Acc* 2005; 113: 233.
60. Aihara J. *Theor Chem Acc* 1999; 102: 134.
61. Aihara J. *J Phys Chem A* 1999; 103: 7487.
62. Scrocco E and Tomasi J. *Adv Quantum Chem* 1978; 103: 115.
63. Spackman MA and Jayatilaka D. *CrystEngComm* 2009; 11: 19.
64. Spackman MA and McKinnon JJ. *CrystEngComm* 2002; 4: 378.
65. Turner MJ, McKinnon JJ, Wolff SK, et al. CrystalExplorer v17.5, University of Western Australia, Perth, WA, Australia, 2017.
66. Rigaku Oxford Diffraction. CrysAlis^{Pro} Software System. Version 1.171.38.43, Rigaku Corporation, Oxford, 2015.
67. Clark RC and Reid JS. *Acta Cryst* 1995; A51: 887.
68. Dolomanov OV, Bourhis LJ, Gildea RJ, et al. *J Appl Cryst* 2009; 42: 339.
69. Sheldrick GM. *Acta Crystallogr Sect* 2015; A71: 3–8.
70. Etter MC, MacDonald JC and Bernstein J. *Acta Crystallogr* 1990; B46: 256.
71. Becke AD. *J Chem Phys* 1993; 98: 1372.
72. Lee C, Yang W and Parr RG. *Phys Rev B* 1988; 37: 785.
73. Frisch MJ, Trucks GW, Schlegel HB, et al. *Gaussian 09 revision D.01*. Wallingford, CT: Gaussian, Inc, 2013.
74. Merrick JP, Moran D and Radom L. *J Phys Chem A* 2007; 111: 11683.
75. Jamroz MH. *Vibrational energy distribution analysis (VEDA 4)*, Warsaw, 2004–2010.
76. GaussView 6.0, Gaussian, Inc., Wallingford, CT, 2016.
77. Foresman JB, Keith TA, Wiberg KB, et al. *J Phys Chem* 1996; 100: 16098.
78. Tomasi J, Mennucci B and Cammi R. *Chem Rev* 2005; 105: 2999.